

Tonal and Broadband Noise Calculations for Aeroacoustic Optimization of Propeller Blades in a Pusher Configuration

Antonio Pagano* Mattia Barbarino† Damiano Casalino‡ Luigi Federico§

CIRA, Italian Aerospace Research Center, Capua, I-81043, Italy

A multi-disciplinary analysis and optimization is carried out for a propeller in a real pusher aircraft configuration with the goal of reducing the radiated noise power levels, while preserving the aerodynamic efficiency. The optimization process involves the shape of the blade and the position of the engine exhaust ducts. A coupling of the unsteady aerodynamic and structural-dynamic blade models provides the aeroelastic propeller model that drives a tonal and broadband aeroacoustic prediction. The tonal noise results from the periodic flow unsteadiness due to the non-axial flight and to the impingement of the engine exhausts on the propeller disk. The broadband noise is mainly due to the interaction between the blade leading-edge and the exhaust turbulence. It is shown that the tonal noise overwhelms the broadband noise, and that the optimization affects the shape of the blade at the tip and in the spanwise segment hit by the exhausts. An overall sound pressure level reduction of 3.5 dB is achieved at the take-off condition, while preserving the design propeller thrust and resulting in a small penalty on the propeller efficiency in cruise.

I. Motivations

IN the framework of the national research project ACADEMIA (Advanced Computational Aerodynamic Environment for Multi-disciplinary Integrated Analysis), the Italian Aerospace Research Center (CIRA) has developed a multi-disciplinary analysis (MDA) and optimization methodology for helicopter rotors and propellers. This methodology was applied in the context of the EC-funded project CESAR (Cost Effective Small Aircraft) to optimize the acoustic and aerodynamic performances of a pusher propeller provided by Piaggio Aero and derived from the propulsive system of the turboprop business aircraft P180.¹ The present work intends to illustrate the subsequent efforts undertaken by CIRA on the methodology improvements and on the extension of the propeller design space.

The P180 is well known in the aeronautical community for its efficiency with respect to small turbojets which operate in the same market sector. Thanks to the rear location of the propeller disks with respect to the passenger seats, the interior noise is lower than for any turbojet or turboprop business aircraft. In return, due to the strongly perturbed flow in which the pusher propellers operate, the exterior noise falls in the upper limit of the acceptable range. The influence of the wing wake and engine exhausts on the noise emitted by the pusher propellers has been investigated in the past both numerically² and experimentally.³ Schematic views of the P180 wing-nacelle configuration are shown in Fig. (1).

Within the CESAR project the main focus was on the application of numerical technologies to design a new propeller able to reduce the noise levels by 3 dB (at least), while preserving good cruise performance characteristics. From preliminary studies it turned out that the original 5-blade propeller could be changed in favour of a 6-blade configuration rotating at a reduced angular velocity. That propeller was selected as baseline configuration for the optimization studies performed by CIRA that led to a modification of the blade planform in the tip region.¹ The analysis involved an aeroelastic and an aeroacoustic model of

*Research engineer, Rotorcraft, Member AIAA.

†Research engineer, Rotorcraft, Member AIAA.

‡Research engineer, Aerodynamic and Aeroacoustic Methods, Member AIAA.

§Research engineer, Rotorcraft, Member AIAA.

the blade that provides the propeller aerodynamic performances and radiated tonal noise to an automatic optimization software. A similar analysis is applied in the present work with the goal of extending the shape optimization to the spanwise segment of the blade hit by the engine exhaust. In addition, the broadband noise generated by the blades is estimated through a semi-analytical model that accounts for the self-noise from the trailing-edge and the blade-turbulence interaction noise from the leading-edge.

As discussed in Ref.,¹ one of the preliminary outcomes of the optimization study was that the 6-blade propeller is 2 dB quieter than the 5-blade one, and that this noise reduction is due to the lower tip speed. Indeed, the prediction of the noise generated by the same isolated propellers revealed that the engine exhausts cause an increase of 9 and 14 dB for the 5- and 6-blade propeller, respectively. This significantly different installation effect is due to the simultaneous blade-exhaust interactions occurring in the 6-blade propeller. For this reason it has been decided to investigate in the present work the effects on the radiated noise due to an angular shift of the exhaust ducts, as sketched in Fig. (1(c)).

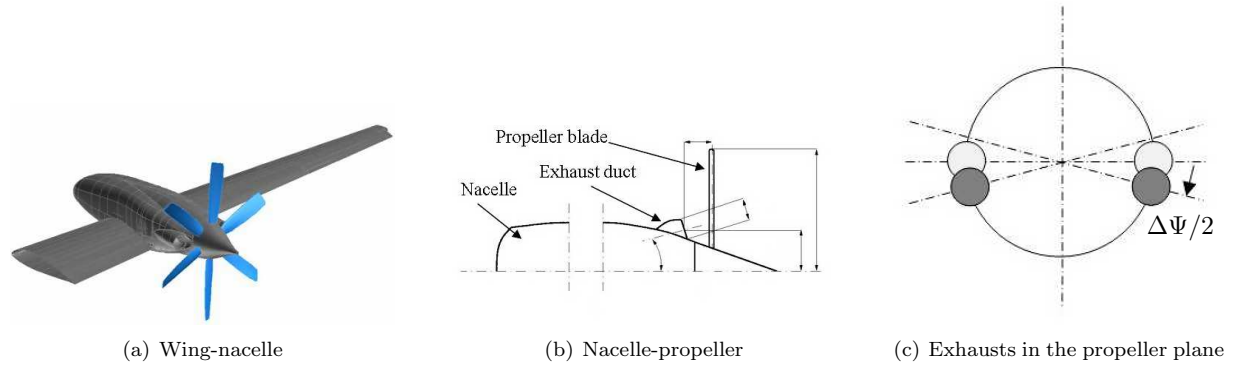


Figure 1. P180 wing-engine system. On the right figure, the baseline and modified exhaust configurations are pictured in light and dark gray, respectively.

The geometric parameterization of a propeller blade results into a large design space. For this reason, a suitable aerodynamic model for automatic optimizations must be sufficiently fast, but able to describe properly the effects due to the rigid and elastic motion of the blade, the compressibility effects at the blade tip, and the aerodynamic losses occurring in the turbulent boundary layers. Hence, it has been decided to employ a rotorcraft full potential CFD model,⁴ strongly coupled with a turbulent boundary layer model based on the "defect formulation theory" developed by Le Balleur.^{5,6} The boundary layer model permits to compute the propeller aerodynamic characteristics and provides the integral quantities required by a semi-analytical broadband noise model. The broadband noise levels are added to the tonal noise levels computed by applying a Ffowcs-Williams & Hawkings acoustic analogy⁷ to the wall pressure distribution.

The layout of the paper is as follows. In section II a general description of the baseline configuration and reference flight conditions is provided. The MDA process and optimization strategy is outlined in section III. Then the elastic, aerodynamic and aeroacoustic models are presented in section V, IV and VI, with emphasis on the broadband noise model that represents the original contribution of this work with respect to the previous one.¹ The results of the optimization study are discussed in section VII, followed by some concluding remarks.

II. Pusher propeller baseline configuration

The baseline configuration has been released by Piaggio Aero after preliminary design studies undertaken in the CESAR project. As sketched in Fig. (1), a 6-blade propeller is considered and its angular velocity is set to 188.5 rad/s, corresponding to a blade passage frequency of 180 Hz. This propeller has been obtained by using the same blade of a 5-blade production propeller that rotates at a higher velocity. Therefore, a shape optimization is required in order to adapt the new propeller to the different operating conditions.

The optimization is carried out by considering two flight conditions: the take-off condition, corresponding to a flight altitude of 914 m and Mach number $M = 0.235$, for which the propulsion system is required to produce a thrust of 6280 N, and the cruise condition, corresponding to a flight altitude of 7620 m and Mach number $M = 0.58$, for which the propulsion system is required to produce a thrust of 2800 N.

As sketched in Fig. (1(c)), the exhaust centerlines are diametrically opposite in the propeller plane. This

is responsible for a higher jet-propeller interaction noise in the case of a 6-blade propeller. It has been therefore decided to estimate the effects of a new exhaust configuration obtained by introducing an angular skew in the two trace disks of the jets in the propeller plane.

III. Optimization process, objectives and constraints

This section is devoted to the description of the MDA process that provides the influence of the blade geometry on the aerodynamic performances and noise of the pusher propeller, and the optimization strategy that drives the MDA process towards a set of blade configurations that meet the required targets, while respecting some geometrical and performance constraints.

III.A. MDA process

In order to compute the noise generated by a pusher propeller with an adequate confidence level, a suitable aeroelastic model of the blade must be matched with an aeroacoustic model. Due to the high flow unsteadiness, mainly caused by the exhaust impinging on the propeller disk and by the elastic blade response, the aeroelastic model of the blade is provided by a weak coupling between a computational structural dynamics (CSD) code and a computational fluid dynamics (CFD) code. The aeroacoustic model extrapolates the blade pressure distribution and boundary layer turbulent quantities into far-field acoustic levels.

The CSD-CFD weak coupling consists of the following steps: (i) the CSD code, for a given thrust coefficient (C_T), provides the first estimation of the pitch angle (θ_{75}), power coefficient (C_P) and efficiency (η); (ii) for the computed value of θ_{75} , the CSD code also provides the blade elastic deformations and the induced velocities on the blade due to the wake structure; (iii) the CFD code accepts in input θ_{75} , the blade elastic deformations and the induced velocities (as an inflow model) and computes the sectional blade aerodynamic coefficients; (iv) the CSD code uses the CFD aerodynamic coefficients (C_l, C_m, C_d) to update the internal 2D aerodynamics so that a new estimate of θ_{75} , C_P and η is provided; (v) a convergence criterion on θ_{75} is checked and, if it is not satisfied, the process control is sent to step (ii).

The aeroacoustic model is based on two distinct approaches, one for the tonal noise, the other one for the broadband noise. The tonal noise is computed from the unsteady blade pressure distribution provided by the CFD code by means of a time-domain integral solution of the FW-H equation,⁷ put forward by Farassat & Succi.⁸ Only the linear source terms due to the unsteady force exerted by the propeller on the surrounding fluid and mass flow displacement due to the blade motion are accounted for. The broadband noise is computed through semi-analytical models that permit to convert statistical flow quantities in proximity of the blade trailing- and leading-edge into far-field noise spectral levels. The near- to far-field extrapolation model is derived from flat-plate unsteady aerodynamic theories and acoustic scattering formula that have been proposed by Amiet and co-workers^{9–12} and successively improved by Roger & Moreau.^{13–15} The near-field flow quantities required by these models are the wall pressure spectrum and boundary layer thickness and asymptotic flow velocity close to the trailing-edge (self-noise), and the velocity spectrum and integral scale of the turbulence convected past the blade leading-edge (turbulence interaction noise).

All the codes and tools involved in the outlined MDA process have been developed by CIRA in the framework of several research programs focused on rotorcraft aerodynamics and aeroacoustics. A brief description of the mathematical formulation implemented in each code is provided in section [V](#), [IV](#) and [VI](#).

III.B. Optimization environment

The commercial optimization tool Optimus¹⁶ developed by Noesisolutions have been used for the present study. This software offers a powerful graphical environment that permits to integrate arbitrary analysis codes, automate the process execution, control the data exchange between multi-disciplinary codes, split the process over a heterogeneous computational environment where analysis codes run on different computer platforms, and post-process the analysis and optimization results. The key functionalities of several optimization methods are fully exploited in order to address the search of global and local optimal solutions. Design of experiment (DOE) and response surface model (RSM) techniques are available for the definition and exploration of the design space. The design optimization can be carried through genetic, gradient and coupled genetic/gradient algorithms.

III.C. Blade shape parameterization

A key element of an efficient automated design optimization of a propeller is the definition of a suitable parametric model of the blade geometry.¹⁷ The general goal is to reduce the number of design variables, while retaining the ability to cover a global range of design solutions. The common approach consists in modeling the blade surface through B-spline or Bézier curves that allow for a large design space, while resulting into a large number of design variables. A different approach is used in this work, which benefits from the choice of keeping the same airfoil shape during the optimization. Therefore only the shape of the blade is modified by varying some constructive parameters of each spanwise section extracted from the original CAD model, say the airfoil chord, twist, sweep and dihedral angles. By acting on these parameters, which can be selected as design variables, it is possible to perturb the blade surface in a continuous way.

In order to reduce the number of design variables, the constructive parameters are prescribed only at three sections of the blade portion to be optimized: the inboard section, the outboard section and a user-defined intermediate section, as sketched in Fig. (2(a)). For a shape optimization over the whole blade the inboard and outboard sections coincide with the root cutout and the blade tip, respectively. Then the blade chord and twist distributions and the leading-edge line are defined using interpolation spline functions involving their values at the prescribed sections. The complete parameterization module is based on 16 parameters, that is, 4 for each of the three considered sections, the spanwise location of the intermediate section, a parameter for setting the type of interpolating function, the blade radius and the propeller angular velocity. As far as the surface and volume grid generation is concerned, a pre-processor module updates the constructive parameters at the prescribed spanwise sections starting from the design variables. Then the surface and volume CFD mesh are regenerated by using transfinite interpolation with suitable exponential blending functions. In Ref.¹ where the outer part of the propeller blade was optimized, 14 design variables were used in the exploration of the design space, while only 6 design variables, the most effective ones, were selected for the multi-objective optimization. In the present work, the region of the blade under the exhaust influence is optimized requiring only 2 parameters, the chord and the twist at the intermediate section. The azimuthal position of the exhaust is used as an additional design variable during the optimization process, as shown in Fig. (2(b)).

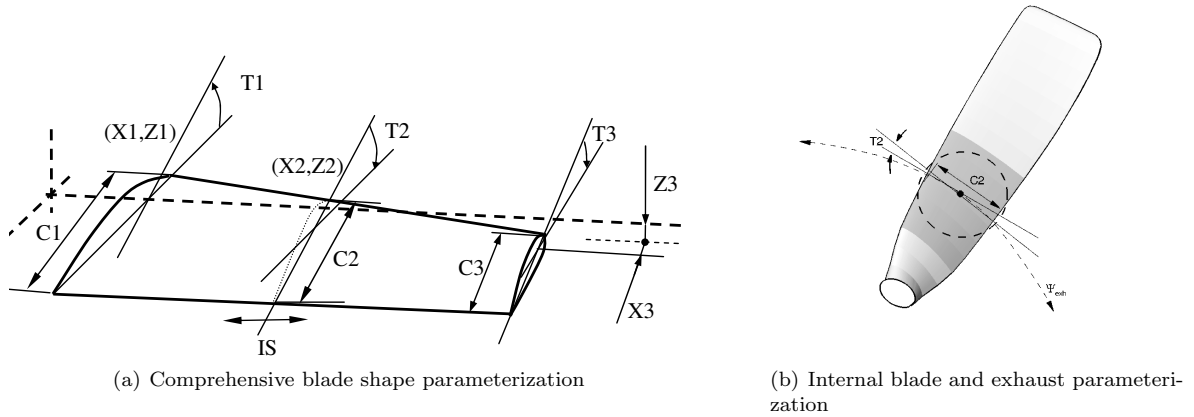


Figure 2. Design variables for the blade propeller optimization problem.

III.D. Constraints

A set of geometrical and performance constraints are considered. The geometrical constraints come from the design space related to the variations of quantities such as built-in twist, sectional chord and leading-edge line definition. In this phase of the design, quite large variations are considered and more stringent constraints, such as those imposed from mould modifications, are left to a subsequent phase. The performance constraints are relative to the shaft power availability, which is set to 633.8 kW for the take-off condition and to 596.6 kW for the cruise condition.

III.E. Multi-objective optimization strategy

The problem under consideration is the optimization of the propeller configuration based on the modification of the blade shape and exhaust position, so that the radiated noise is reduced at take-off condition and the aerodynamic performances at cruise condition are not downgraded. The order in which the objectives are presented also reflects a priority in the sense that it is desirable to address both these objectives, however, while the primary necessity is to reduce the noise impact, small gains in efficiency or even small performance degradations could be accepted. The opposite situation, that is, an increase in aerodynamic efficiency resulting in a noisier configuration, is not allowed.

The proper way to address this multi-objective optimization problem consists in finding a vector of design variables so that a vector of objective functions is minimized, while a set of geometric/performance constraints bounds the problem. The process converges towards a family of optimal solutions, clustered around the so-called Pareto front in the space of the design variables. The choice of the design optimal solution then relies on a trade-off between the conflicting objectives.

In Ref.¹ it was emphasized that the exhaust had a limited aerodynamic influence on the outer part of the blade. In practice, the sudden and strong variation of the blade loads in the exhaust region was not observed in the outer part of the blade ($r/R > 0.75$). This has suggested to decouple the optimization of the inboard part of the blade from the outer part with the major advantage of retaining the outcome of the optimization work already performed. Thus, the optimization strategy pursued in this work is based on the following steps: (i) a DOE investigation of the blade inner part is carried out with a twofold aim, the outline of the most promising regions of the design space, and the preparation of a database for the construction of the response surface; (ii) an optimization based on evolutionary algorithms and exploiting the RSM is applied in order to select an optimal design; (iii) the full MDA process is used in order to analyze the optimal design and thus verify that the RSM-predicted gains are confirmed; (iv) the azimuthal position of the exhausts is modified and the corresponding noise levels are computed; (v) if the inboard blade shape and the exhaust azimuthal position provide separately a noise reduction, a further optimization is carried out starting from a hybrid blade incorporating the shape modifications obtained in Ref.¹ and step (ii), and using the full MDA process.

IV. Aerodynamic model

The CFD code used in the present study is HELIFPX,¹⁸ developed in the framework of the EC-funded project ROSAA¹⁹ and further improved by CIRA. It is an unsteady aerodynamic potential flow solver based on a zonal approach in which an inviscid full potential model, a boundary layer module, a viscous-inviscid interaction method and a grid generator are integrated to model the flow about complex multi-bladed rotors.

The most relevant features of HELIFPX are: (i) the governing equations are cast in conservative form in the inertial frame of reference; (ii) a streamwise density flux biasing is applied in order to avoid non-physical solutions (expansion shocks) and to stabilize the computation in supersonic flow regions; (iii) entropy and vorticity corrections are implemented taking into account, respectively, shock-generated entropy and vorticity; (iv) the equation is discretized so that the resulting numerical scheme is 1st order in time and 2nd order in space for subsonic regions and 1st order in space for supersonic regions; (v) the discretized equation is solved using an approximate factorization (AF3) technique with upwinding in supersonic regions.

The code takes advantage of the strong viscous-inviscid coupling with a boundary layer internal module which is based on the thin-layer approximation of the Navier-Stokes equations by means of the Le Balleur's "defect formulation theory".^{5,6,20,21} This original formulation splits the system of Reynolds-averaged Navier-Stokes (RANS) equations at all points in two exactly equivalent systems: the viscous defect-formulation system and the pseudo-inviscid flow system, both being solved in the same physical domain. The numerical viscous-inviscid strong coupling algorithm consists in correcting the inviscid field using a wall mass flux calculated by the viscous solver and implemented through a transpiration velocity technique. Iterations between the viscous solution and the full-potential field are performed at each time-step and at each coupling node both on the wall and the wake branch. Moreover, the code makes use of a Clebsch variable model²² to take into account the generation of vorticity caused by strong shock waves that violate the irrotational assumption of the potential formulation. For the sake of the present work, which is focused on the MDA process rather than the specifics of each involved discipline, only the underlying elements of the full potential flow model and numerical discretization are provided, followed by validation tests carried out for a transonic propeller configuration and a helicopter rotor.

Consider a compressible inviscid perfect isentropic irrotational gas mean flow, so that $c^2 = \gamma p / \rho = \gamma R T$, where γ and R are the ratio of heats and the gas constant, respectively, and c , p , ρ and T are the flow sound speed, pressure, density and temperature, respectively. The hypothesis of irrotational flow allows to introduce the velocity potential ϕ , so that $\mathbf{v} = \nabla \phi$. The flow dynamics is therefore described by the continuity equation $\rho_t + \nabla \cdot (\rho \mathbf{v}) = 0$ and by the generalized Bernoulli's equation $c^2 = 1 - (\gamma - 1) (\phi_t + v^2/2)$, the subscript t denoting partial time derivative. By introducing a generalized coordinate system (ξ, η, ζ, τ) fixed with the body, the governing equations can be written as:

$$(\rho/J)_t + \nabla \cdot (\rho \mathbf{Q}/J) = 0 \quad (1)$$

$$c^2 = 1 - (\gamma - 1) [\phi_t + (\mathbf{Q} + \boldsymbol{\sigma}_t) \cdot \nabla \phi / 2] \quad (2)$$

where $\mathbf{Q} = \boldsymbol{\sigma}_t + H H^T \nabla \phi$ is the contravariant velocity vector, H is the Jacobian matrix of the coordinate transformation, J is the determinant of H and $\boldsymbol{\sigma}_t = H \mathbf{x}_t$ is the apparent velocity vector. Eq. (1) is discretized in time by means of an implicit scheme leading to the linear system $L(\phi^{n+1} - \phi^n) = R$, where:

$$L = \left\{ I + \Delta \tau \mathbf{Q} \cdot \nabla - \frac{\Delta \tau^2 c^2 J}{\rho} \left[\frac{\partial}{\partial \xi} \left(\frac{\rho g_{11}}{J} \right) \frac{\partial}{\partial \xi} + \frac{\partial}{\partial \eta} \left(\frac{\rho g_{22}}{J} \right) \frac{\partial}{\partial \eta} + \frac{\partial}{\partial \zeta} \left(\frac{\rho g_{33}}{J} \right) \frac{\partial}{\partial \zeta} \right] \right\} \quad (3)$$

$$R = \Delta \tau^2 \left(\frac{c^2 J}{\rho} \right)^n \left[\frac{\left(\frac{\rho}{J} \right)^n - \left(\frac{\rho}{J} \right)^{n-1}}{\Delta \tau} + \nabla \cdot \left(\frac{\rho^* \mathbf{Q}}{J} \right)^n \right] + (\phi^n - \phi^{n-1}) \\ + \Delta \tau \left(\frac{\rho}{c^2 J} \right)^{n-1} \left(\frac{c^2 J}{\rho} \right)^n \left[\frac{\phi^n - 2\phi^{n-1} - \phi^{n-2}}{\Delta \tau} + \mathbf{Q}^{n-1} \cdot \nabla (\phi^n - \phi^{n-1}) \right] \quad (4)$$

with g_{11} , g_{22} and g_{33} denoting the diagonal elements of the metric tensor $H H^T$, and ρ^* the so-called retarded density, which provides an entropy fix condition. As suggested in Refs.,^{23,24} the time derivative $(\rho/J)_\tau$ for deforming grid applications can be computed by exploiting the formula $(\rho/J)_\tau = \rho_\tau / J - \rho \left[(\xi_t/J)_\xi + (\eta_t/J)_\eta + (\zeta_t/J)_\zeta \right]$.

HELIFPX has been fully validated against experimental data, mainly coming from wind tunnel campaigns on rotary wings carried out during several European projects. Among others, two validation cases are described hereafter. The first one is the so-called "low speed propeller" of the SNAAP project.²⁵ It is a 6-blade transonic propeller of radius $R = 0.4495$ m advancing at a Mach number of 0.7 and rotating at an angular velocity of 410.7 rad/s. Fig. (3) shows the effect of the Clebsch correction on the chordwise shock location at different radial stations. A fairly good agreement with the experimental data is obtained in terms of pressure coefficient. The second validation case is the EC/ONERA 7A rotor experimentally investigated in the HELISHAPE project.²⁶ The rotor of radius $R = 2.1$ m operates at a medium speed forward and level flight with advance ratio $\mu = 0.355$, thrust coefficient $C_T = 0.0071$ and rotational velocity $M_{\omega R} = 0.616$. Fig. (4) shows the pressure coefficient at the radial station $r/R = 0.92$ and at different azimuthal locations. The numerical results obtained with increasing physical sophistication level exhibit a consistent behaviour, the better results being obtained by using a viscous flow model and an elastic blade. The same trend is confirmed by the normal force coefficient at different radial stations plotted in Fig. (5).

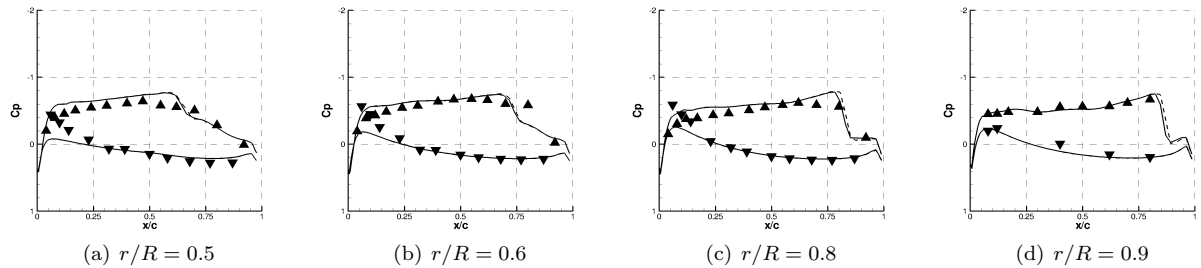


Figure 3. Pressure coefficient at different radial stations for the SNAAP propeller. Experimental data (symbols), full-potential + entropy correction (dashed line), full-potential + entropy and vorticity (Clebsch) corrections (solid line).

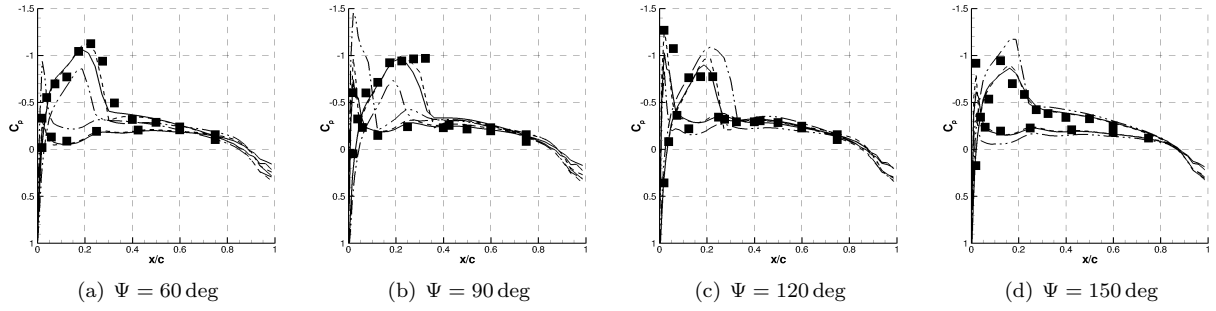


Figure 4. Pressure coefficient at the radial station $r/R = 0.92$ and different azimuthal locations for the EC/ONERA 7A rotor. Experimental data (symbols), inviscid-flow/rigid-blade results (dashed-dotted line), inviscid-flow/elastic-blade results (dashed line), viscous-flow/elastic-blade results (solid line).

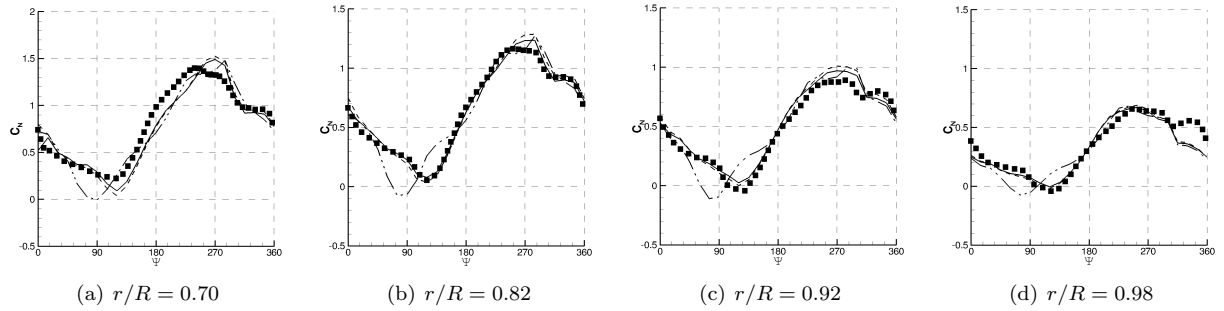


Figure 5. Normal force coefficient at different radial stations for the EC/ONERA 7A rotor. Experimental data (symbols), inviscid-flow/rigid-blade results (dashed-dotted line), inviscid-flow/elastic-blade results (dashed line), viscous-flow/elastic-blade results (solid line).

V. Structural-dynamic model

The propeller structural dynamic model is provided by the multi-body CSD code HELTRIM. Its formulation allows to account for mutual interaction effects due to blade aerodynamics, rigid motion and twist deformation. The local unsteady aerodynamic forces and moments are predicted using indicial formulation²⁷ and the induced velocity field is evaluated using the Mangler & Squire inflow model,²⁸ which makes use of the incompressible linearized Euler equation to relate the pressure field across the disk plane to the induced velocity distribution. A finite element discretization of the torsional variational problem is used in order to compute the blade deformation induced by simple twisting. The embedded aerodynamic model can be replaced by a coupling with a CFD code, as carried out in the present work.

Since the purely CSD formulation can be verified through elementary numerical tests, it is more interesting to report the results of a validation test of the coupled CSD-CFD model. Experimental data from wind tunnel measurements undertaken in the framework of the EC-funded project HeliNOVI²⁹ are used. The test case is a BO105 helicopter wind tunnel model having a radius scale factor of 2.456 and a rotor angular speed of 110 rad/s. As shown in Fig. (6(a)), the use of a more accurate aerodynamic model provided by the coupling with the CFD code, results in a significant improvement of the numerical prediction. The CSD-CFD coupling usually converges within 4-5 iterations as illustrated in Fig. (6(b)) where the behaviour of the pitch and flapping angle, both expressed in terms of their mean and 1st harmonic values, is plotted.

VI. Aeroacoustic model

The aeroacoustic model used in the present study consists of two distinct tools, the first one providing the noise signals from the computed unsteady CFD solution and body kinematics, the second one computing the noise spectra due to turbulence in proximity of the leading-edge (ingested turbulence) and trailing-edge (boundary-layer turbulence). Since the CFD solution accounts for the periodic flow unsteadiness due to the non-axial flight and jet-propeller interaction, the first tool is used to compute the tonal part of the radiated noise. On the contrary, the second tool exploits a statistical representation of the turbulent fluctuations

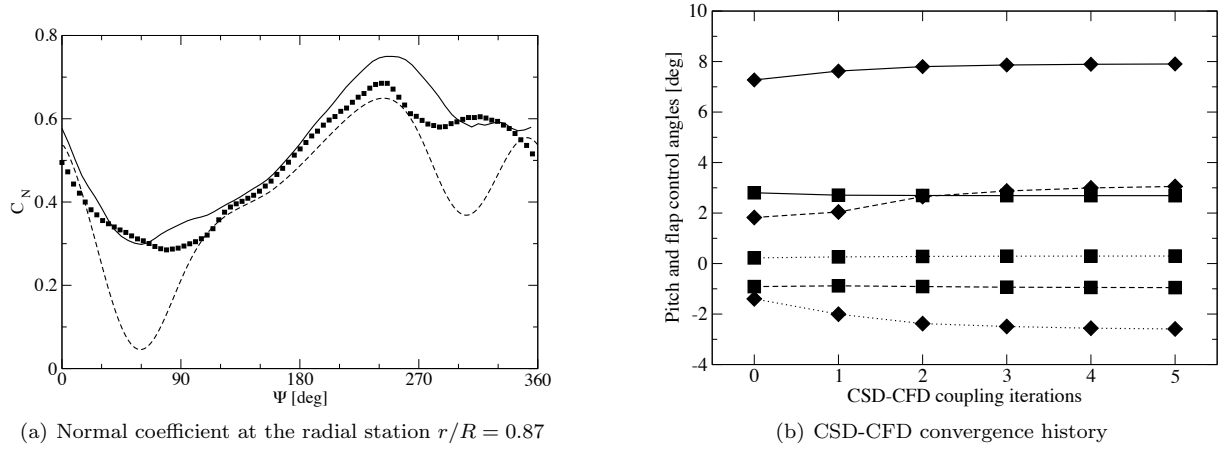


Figure 6. HeliNOVI BO105 low speed climb test case (advance ratio $\mu = 0.15$), climb angle $\tau = 12$ deg. On the left, comparison between experimental data (symbols), CSD prediction (dashed line), and CSD-CFD coupled prediction (solid line). On the right, convergence behaviour of the pitch angle (diamond symbols) and flap angle (square symbols) in terms of their mean values (solid line), 1st harmonic cosine term (dashed line) and 1st harmonic sine term (dotted line).

about the propeller blades and is therefore suited for estimating the broadband noise levels.

VI.A. Tonal noise

The tonal noise generated by the propeller is computed by means of the FW-H solver OLA³⁰ (Object-oriented Library for Aeroacoustics). OLA has been recently developed at CIRA by rewriting in the C++ language all the older tools based on Kirchhoff and FW-H formulations,^{31,32} and by adding two new functionalities: the porous formulation,^{33,34} and the marching cube algorithm for supersonic rotating domains.³⁵

For the sake of the present study, the retarded-time formulation 1A⁸ is employed, and the linear terms, the so-called thickness and loading noise contributions, are computed through integrals on the blade surface. The quadrupole contribution due to the non-linear terms distributed in the perturbed field around the blade is neglected. The linear terms read:

Thickness noise:

$$4\pi p'_T(\vec{x}, t) = \iint_S \left[\frac{\rho_0 (\dot{V}_n + V_n)}{r(1 - M_r)^2} \right]_{\text{ret}} dS_y + \iint_S \left[\frac{\rho_0 V_n (r\dot{M}_r + c_0(M_r - M^2))}{r^2(1 - M_r)^3} \right]_{\text{ret}} dS_y \quad (5)$$

where $r = |\mathbf{x} - \mathbf{y}(\tau)|$ is the source-to-observer distance, \vec{M} of magnitude M is the Mach number vector of a source point on the blade surface S , which moves with an outward normal velocity V_n . The dotted quantities denote time derivative with respect to the source (retarded) time $\tau = t - |\mathbf{x} - \mathbf{y}(\tau)|/c_0$. M_r is the projection of \vec{M} in the observer direction. Quantities in the square brackets are evaluated at the retarded time. The subscripts a , n and r denote, respectively, quiescent fluid quantities, quantities projected along the surface normal direction $\hat{\mathbf{n}}$, and quantities projected along the source-to-observer direction.

Loading noise:

$$4\pi p'_L(\vec{x}, t) = \frac{1}{c_0} \iint_S \left[\frac{\dot{F}_r}{r(1 - M_r)^2} \right]_{\text{ret}} dS_y + \iint_S \left[\frac{F_r - F_M}{r^2(1 - M_r)^2} \right]_{\text{ret}} dS_y + \frac{1}{c_0} \iint_S \left[\frac{F_r (r\dot{M}_r + c_0(M_r - M^2))}{r^2(1 - M_r)^3} \right]_{\text{ret}} dS_y \quad (6)$$

where $\vec{F} = (p - p_0) \hat{\mathbf{n}}$ is the pressure force acting on the surface S , and F_M is the pressure force projected along the direction of the surface motion.

The thickness and loading noise terms provided by OLA have been verified for the more generic case of an integration upon a porous surface. The verification approach is the same as the one outlined in Ref.³⁶ It permits to verify the acoustic extrapolation of a perturbed near field against exact analytical solutions.

Both the integrand fluctuating quantities and the far-field acoustic signals perceived by an arbitrarily moving observer are computed analytically by using elementary sources in arbitrary motion inside a moving integration surface. The test case is pictured in Fig. (7(a)) and the corresponding noise signals are plotted in Fig. (7(b)). The same space-time discretization as for test case J of Ref.³⁶ has been used. The relative L_2 error with respect to the analytical solution is $5.3 \cdot 10^{-3}$, which is slightly higher than the reference value of $4.2 \cdot 10^{-3}$. The difference is probably due to the different numerical integration: a 1st order integration is used in OLA, whereas a 2nd order Gaussian quadrature was used in the reference code.

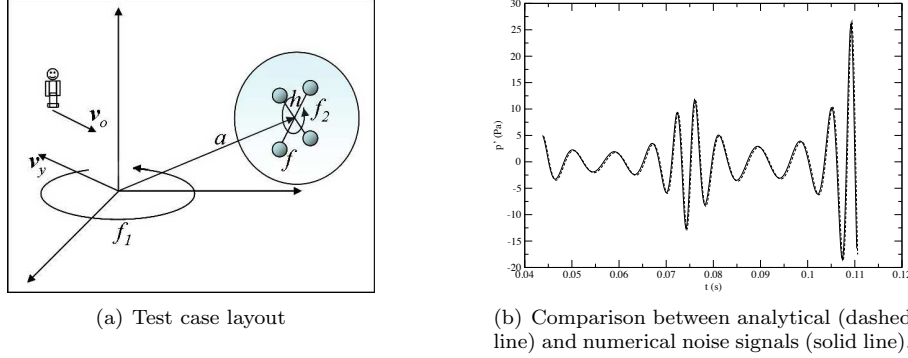


Figure 7. Verification test of the code OLA. Four equal monopoles of magnitude $Q = 0.1 \text{ kg/s}$ and frequency $f = 110 \text{ Hz}$ are located on the vertices of a square and rotate around the square axis at the frequency $f_2 = 43 \text{ Hz}$, and around a perpendicular axis at the frequency $f_1 = 20 \text{ Hz}$. The whole system translate at the velocity $\mathbf{v}_y = (50, 40, 30) \text{ m/s}$, while the observer translates at the velocity $\mathbf{v}_o = (-10, -30, -50) \text{ m/s}$. The surface integration is performed upon a sphere that rotates around the vertical axis at the frequency f_1 . The two radii have values $a = 1 \text{ m}$ and $h = 0.1 \text{ m}$. The initial position of the observer is set to $\mathbf{x} = (10, 10, 10) \text{ m}$.

VI.B. Broadband noise

The code used for the propeller broadband noise prediction is TELE-Noise recently developed at CIRA for both rotorcraft and airframe noise applications. The code is based on semi-analytical models of the noise generated by the hydrodynamic pressure fluctuations induced by the boundary layer turbulence in the neighborhood of a trailing-edge, and by the interaction between freestream turbulence convected past a leading-edge. In both cases, the turbulent fluctuations can be obtained by solving the full resolved or filtered Navier-Stokes equations, and then propagated to the far-field through the FW-H integral approach outlined in § VI.A. This approach, however, can be used only for research purposes. A viable alternative consists in using analytical models that relates near field statistical quantities provided by a RANS solution, to the statistics of the acoustic far field. Although derived from exact solutions of flat-plate acoustic scattering problems, these models can be applied to realistic geometries like wings and rotating blades. The formulation herein reported follows from the original works of Amiet and co-workers^{9–12} and Roger & Moreau.^{13–15}

VI.B.1. Trailing-edge noise

Consider a blade section of chord c and span length L , as sketched in Fig. (8(a)). The mean flow is parallel to the x direction. The noise power spectral density reads:

$$S_{pp}^{\text{TE}}(x, y, z, \omega) = \left(\frac{\bar{k}z}{2\pi\sigma^2} \right)^2 2c \int_{-\infty}^{\infty} \Phi_{pp} \left(\frac{\omega}{U_c}, k_y \right) \frac{\sin^2 \left[\frac{L}{c} \left(\bar{k}_y - \bar{k}_y/\sigma \right) \right]}{\left(\bar{k}_y - \bar{k}_y/\sigma \right)^2} \left| I^{\text{TE}} \left(\frac{\bar{k}}{U_c}, \bar{k}_y \right) \right|^2 d\bar{k}_y \quad (7)$$

where $\bar{k} = \omega c / (2c_0)$ is the non-dimensional acoustic wavenumber, $\sigma = \sqrt{x^2 + \beta^2(y^2 + z^2)}$ is the Prandtl-Glauert transformed distance from the trailing-edge ($\beta = \sqrt{1 - M^2}$), Φ_{pp} is the wall pressure wavenumber-frequency spectrum, U_c is the boundary layer eddy convection velocity, $\bar{k}_y = k_y c / 2$ is the non-dimensional wavenumber in the spanwise direction, and I^{TE} is the radiation integral function. This consists of a main contribution I_1^{TE} derived from the assumption of a semi-infinite flat plate (high frequency approximation), and a term I_2^{TE} accounting for the wave back reflection at the leading-edge (finite chord length correction).

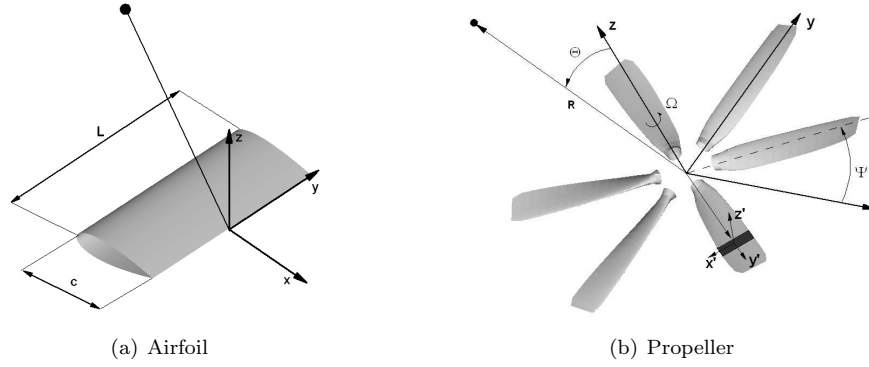


Figure 8. Coordinate systems and notation used for the airfoil broadband noise model and extension to a propeller configuration.

These read:

$$I_1^{\text{TE}} = \frac{i e^{2iC}}{C} \left\{ (1+i) e^{-2iC} \sqrt{\frac{B}{B-C}} E^*(2B-2C) - (1+i) E^*(2B) + 1 \right\} \quad (8)$$

$$I_2^{\text{TE}} = H \left\{ e^{4i\bar{\kappa}} [1 - (1+i) E^*(4\bar{\kappa})] \right\}^\varepsilon + H \left[-e^{2i\Theta^-} + i (\Theta^- + \bar{k}_x + M\bar{\mu} - \bar{k}) G \right] \quad (9)$$

where $\bar{k}_x = k_x c/2$ is the non-dimensional wavenumber in the streamwise direction, $M = U_0/c_0$ is the mean flow Mach number, $\bar{\mu} = \omega c/(2c_0\beta^2)$, $E^*(\xi) = \int_0^\xi e^{-it}/\sqrt{2\pi t} dt$ is the Fresnel integral, and the notation $\{\}^\varepsilon$ means that the imaginary part must be multiplied by a factor $\varepsilon = 1/\sqrt{1+1/(4\bar{\kappa})}$. The other functions are defined as follows:

$$\begin{aligned} B &= \bar{K}_x - M\bar{\mu} + \bar{\kappa}, \quad C = \bar{K}_x - \bar{\mu}(x/\sigma - M), \quad H = \frac{(1+i) e^{-4i\bar{\kappa}} (1 - \Theta^2)}{2\sqrt{\pi} (\alpha - 1) \bar{k}_x \sqrt{B}}, \quad \Theta^- = \bar{\kappa} - \bar{\mu}x/\sigma \\ G &= (1+\varepsilon) e^{i(2\bar{\kappa}+\Theta^-)} \frac{\sin(\Theta^- - 2\bar{\kappa})}{\Theta^- - 2\bar{\kappa}} + (1-\varepsilon) e^{i(-2\bar{\kappa}+\Theta^-)} \frac{\sin(\Theta^- + 2\bar{\kappa})}{\Theta^- + 2\bar{\kappa}} \\ &+ \frac{(1+\varepsilon)(1-i)}{2(\Theta^- - 2\bar{\kappa})} e^{4i\bar{\kappa}} E^*(4\bar{\kappa}) - \frac{(1-\varepsilon)(1+i)}{2(\Theta^- + 2\bar{\kappa})} e^{-4i\bar{\kappa}} E(4\bar{\kappa}) \\ &+ \frac{e^{2i\Theta^-}}{2} \sqrt{\frac{2\bar{\kappa}}{\Theta^-}} E^*(2\Theta^-) \left[\frac{(1-\varepsilon)(1+i)}{\Theta^- + 2\bar{\kappa}} - \frac{(1+\varepsilon)(1-i)}{\Theta^- - 2\bar{\kappa}} \right] \end{aligned} \quad (10)$$

where $\bar{\kappa}^2 = \bar{\mu}^2 - \bar{k}_y^2/\beta^2$, $\bar{K}_x = \omega c/(2U_c)$, and $\alpha = U_0/U_c$ is the ratio between the boundary layer asymptotic velocity and the eddy convection velocity. The wall pressure wavenumber-frequency spectrum $\Phi_{pp}(\omega/U_c, k_y)$ in Eq. (7) can be related to the wall pressure power spectral density $\phi_{pp}(\omega)$ and to the coherence $\gamma(\eta_y, \omega)$ between two points separated by the spanwise distance η_2 through the relationship $\Phi_{pp}(\omega/U_c, k_y) = \phi_{pp}(\omega) l_y(\omega, k_y)/\pi$, with $l_y(\omega, k_y) = \int_0^\infty \gamma(\eta_y, \omega) \cos(k_y \eta_2) d\eta_2$. The spanwise correlation length is assumed to be given by the Corcos' formula $l_y(\omega, k_y) = bU_c/\omega$, with b being a calibration constant. The power spectral density $\phi_{pp}(\omega)$ can be estimated through a semi-empirical model proposed by Rozenberg³⁷ that takes into account the chordwise pressure gradient, i.e.:

$$\phi\left(\frac{\omega\delta^*}{U_0}\right) = \frac{(\tau_w^2\delta^*/U_0) 0.78(1.8\Pi\beta_c + 6) (\omega\delta^*/U_0)^2}{\left[(\omega\delta^*/U_0)^{0.75} + 0.105\right]^{3.7} + [3.76Re_T^{-0.57} (\omega\delta^*/U_0)]^7} \quad (11)$$

where δ^* denotes the boundary layer displacement thickness, τ_w is the wall shear stress, $Re_T = u_\tau \delta \sqrt{C_f/2}/\nu$ is the weighted Reynolds number, u_τ being the friction velocity, $\beta_c = (\theta/\tau_w) dp/dx$ is the Clauser's pressure gradient parameter, θ being the boundary layer momentum thickness, and Π is the wake law parameter resulting from $2\Pi - \ln(1+\Pi) = \kappa U_0/u_\tau - \ln(\delta^* U_0/\nu) - 0.51\kappa - \ln \kappa$, $\kappa = 0.41$ being the von Kármán constant.

VI.B.2. Leading-edge noise

Consider the airfoil configuration sketched in Fig. (8(a)), with the reference system centered at the leading-edge. The far-field noise spectral density due to impinging turbulent fluctuations can be written as:

$$S_{pp}^{\text{LE}}(x, y, z, \omega) = \left(\frac{\rho_0 \bar{k} z}{\sigma^2} \right)^2 \pi U_0 \frac{L}{2} \int_{-\infty}^{\infty} \Phi_{ww} \left(\frac{\omega}{U_0}, k_y \right) \frac{\sin^2 \left[\frac{L}{2} \left(\frac{k_y}{\sigma} - k_y \right) \right]}{\frac{\pi L}{2} \left(\frac{k_y}{\sigma} - k_y \right)^2} \left| I^{\text{LE}} \left(x, \frac{\omega}{U_0}, k_y \right) \right|^2 dk_y \quad (12)$$

where the radiation integral I^{LE} takes into account both the main leading-edge contribution I_1^{LE} and the trailing-edge back scattering contribution I_2^{LE} that are given by:

$$I_1^{\text{LE}} = -\frac{1}{\pi} \sqrt{\frac{2}{(\bar{k}_x + \beta^2 \bar{\kappa})}} \Theta^- e^{-i\bar{\Theta}} E(2\Theta^-) \quad (13)$$

$$I_2^{\text{LE}} = \frac{e^{-i\bar{\Theta}}}{\pi \Theta^- \sqrt{2\pi (\bar{k}_x + \beta^2 \bar{\kappa})}} \left\{ i \left(1 - e^{2i\Theta^-} \right) - (1 + i) \left[E(4\bar{\kappa}) - e^{2i\Theta^-} \sqrt{\frac{2\bar{\kappa}}{\Theta^+}} E(2\Theta^+) \right] \right\} \quad (14)$$

where $\Theta^\pm = \bar{\kappa} \pm \bar{\mu}x/\sigma$, and $\bar{\Theta} = \bar{k}_x (1 - Mx/\sigma) / \beta^2 - \pi/4$. The velocity wavenumber-frequency spectrum of the impinging upward velocity $\Phi_{ww}(\omega/U_0, k_y)$ can be related to the velocity power spectral density $\phi_{ww}(\omega)$ and spanwise correlation length $l_y(\omega, k_y)$ through the relationship $\Phi_{ww}(\omega/U_0, k_y) = U_0 \phi_{ww}(\omega) l_y(\omega, k_y) / \pi$. Then, the impinging turbulent fluctuations can be modeled as frozenly convected homogeneous isotropic turbulence ($\omega = k_x U_0$) described by a von Kármán spectrum, i.e.:

$$\phi(k_x) = \frac{\overline{u'^2} L_t}{2\pi U_0} \frac{1 + \frac{8}{3} (k_x/k_e)^2}{\left[1 + (k_x/k_e)^2 \right]^{11/6}}, \quad \text{and} \quad l_y(k_x) = \frac{8L_t}{3} \left[\frac{\Gamma(1/3)}{\Gamma(5/6)} \right]^2 \frac{(k_x/k_e)^2}{\left[3 + 8 (k_x/k_e)^2 \right] \sqrt{1 + (k_x/k_e)^2}} \quad (15)$$

where $k_e = (\sqrt{\pi}/L_t) \Gamma(5/6) / \Gamma(1/3)$ is the wavenumber of maximum turbulent kinetic energy, Γ is the gamma function, $\overline{u'^2}$ is the mean square value of the turbulent velocity fluctuations and L_t is turbulence integral scale. Both $\overline{u'^2}$ and L_t can be related to the Reynolds-averaged turbulent kinetic energy K and dissipation rate ϵ by writing $\overline{u'^2} = 2K/3$ and $L_t = 0.4K^{1.5}/\epsilon$.

VI.B.3. Broadband noise models validation

The trailing-edge noise model can be validated by using the airfoil self-noise data collected by Brooks & Hodgson.³⁸ A NACA-0012 airfoil of chord $c = 0.6096$ m and span $L = 0.46$ m at zero incidence is considered, for two free-stream velocities: $U_0 = 69.5$ m/s and $U_0 = 38.6$ m/s. The measured boundary layer quantities are: $\delta^* = 4 \cdot 10^{-3}$ m and $U_c = 0.6 U_0$, for both cases, and $b = 1.724$ and $b = 1.613$ for the higher and lower free-stream velocity, respectively. The sound pressure levels at a distance of 1.2 m from the trailing-edge are shown in Fig. (9(a)). The higher vales curves correspond to the higher free-stream velocity. The semi-analytical results have been obtained by using two different approaches: the first one consists in using the measured wall pressure spectrum and spanwise correlation length close to the trailing-edge, the second one consists in using the Rozenberg's semi-empirical wall pressure spectrum model computed on the base of the boundary-layer quantities provided by the Le Balleur's thin-layer viscous model of the CFD code HELIFPX. Therefore, the second approach provides a full validation of the aeroacoustic broadband noise model employed in the present work. It can be observed that both the frequency and velocity trends of the noise levels are quite well predicted, which is mostly relevant for an optimization process. Furthermore, the noise levels are predicted with an accuracy of about 3–4 dB. Indeed, the underestimation of the noise levels is likely to be due to the fact that Brooks & Hodgson measured both the airfoil trailing-edge noise and the jet-turbulence interaction noise that should have roughly the same levels, thus justifying a factor 2 in the noise prediction.

The leading-edge noise model can be validated by using the airfoil turbulence interaction noise data collected by Paterson & Amiet.¹⁰ A NACA-0012 airfoil of chord $c = 0.23$ m and span $L = 0.53$ m at zero incidence and five free-stream velocities in the range 40-165 m/s is considered. The sound pressure levels at a distance of 2.25 m from the leading-edge are shown in Fig. (9(b)). The semi-analytical results have been

obtained by assuming the measured turbulence intensity and integral length scale, and taking into account the shear layer refraction effects. Again, it is worthwhile to observe that the frequency and velocity trends of the noise levels are quite well predicted, and that the confidence level of the prediction is about 3 dB in the maximum noise frequency range.

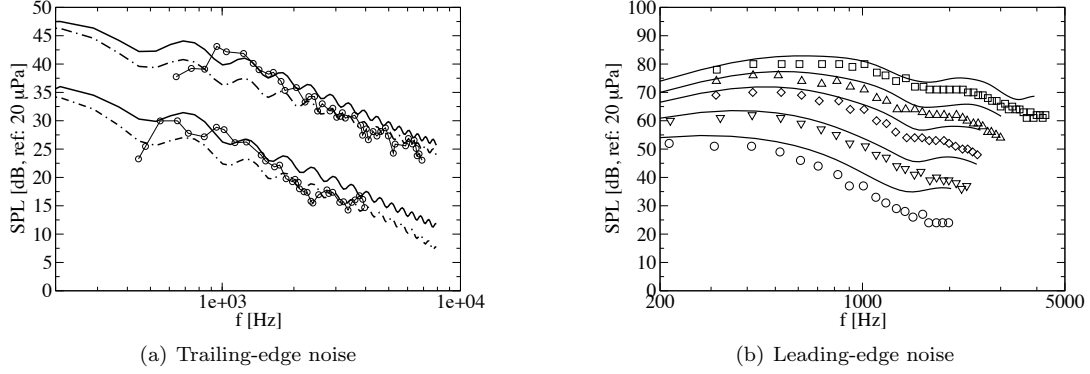


Figure 9. Airfoil broadband noise results. On the left, NACA-0012 self-noise measurements³⁸ (symbols) are compared to semi-analytical results obtained by using the measured wall pressure spectrum (solid line) and the semi-empirical computed wall pressure spectrum (dashed-dotted line). On the right, NACA-0012 interaction-noise measurements¹⁰ (symbols) are compared to semi-analytical results (lines) at different free-stream velocities (\square : 165 m/s, \triangle : 120 m/s, \diamond : 90 m/s, ∇ : 60 m/s, \circ : 40 m/s).

VI.B.4. Extension to a rotating blade

In order to extend the airfoil broadband noise models to a propeller blade, a strip theory is applied. The blade is segmented in a number of spanwise elements, as shown in Fig (8(b)), and for each of them the corresponding 2D mean-flow, turbulent quantities and radiation angles are extracted from the HELIFPX solution file. In addition, a frequency-shift correction is applied to each section in order to account for the Döppler effects by writing $\omega_e(\Psi)/\omega = 1 + M_t \sin \Theta \sin \Psi / \sqrt{1 - M_z^2 \sin^2 \Theta}$, M_t and M_z being the tip and axial Mach numbers of the blade section, respectively. Finally, the overall propeller noise is computed by assuming fully uncorrelated strip sources and averaging over all the angular positions of the B propeller blades, i.e.:

$$S_{pp}(\mathbf{x}, \omega) = \frac{B}{2\pi} \int_0^{2\pi} \frac{\omega_e(\Psi)}{\omega} S_{pp}^\Psi(\mathbf{x}, \omega_e) d\Psi \quad (16)$$

VII. Optimization results

Before addressing the optimization problem it is interesting to assess the different tonal and broadband competing noise mechanisms for the reference pusher propeller configuration. Fig. (10) shows the sound pressure noise directivity patterns computed at a certain distance from the propeller center on a plane containing the propeller axis that corresponds to the radiation angle 90 deg.

The broadband noise contributions plotted in Figs. (10(a)) and (10(b)) have been computed for the installed baseline propeller by feeding TELE-Noise with the mean-flow and boundary-layer quantities computed by HELIFPX. Furthermore, the interaction noise has been computed by estimating the exhaust turbulence level and integral scale by means of a separate RANS jet simulation: an axi-symmetric jet at the same exhaust conditions has been considered and the average levels of K and ϵ have been extracted at the same nozzle/propeller distance. Along the angular sectors for which no blade-exhaust interaction occurs, typical values of ingested atmospheric turbulence have been used. The tonal noise contributions have been computed by considering an isolated propeller, for which the only significant unsteady mechanism is due to the non-axial flight speed, and the installed propeller, for which the dominant unsteady mechanism is due to the blade-exhaust interaction. It is interesting to observe that the overall broadband noise is about 40 dB higher than the trailing-edge noise, and that the tonal noise generated by the installed propeller overwhelms both the broadband noise and the tonal noise in the absence of blade-exhaust interactions (apart the BPF peak).

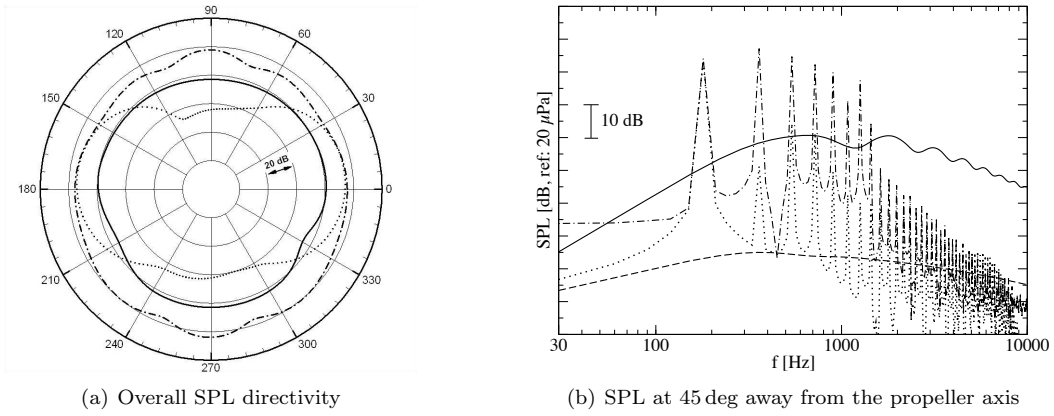


Figure 10. Computed propeller noise directivity patterns and SPL spectra ($\Delta f = 30$ Hz). Comparison between: tonal noise (dashed-dotted line), tonal noise with no exhaust (dotted line), overall broadband noise (solid line), and trailing-edge noise (dashed line).

Therefore, it can be reasonably asserted that the optimization process presented hereafter is mostly driven by the minimization of the tonal noise.

In Ref.¹, an optimized blade, here referred to as "*optim-1*", was obtained, providing a reduction of 1.5 dB of the acoustic energy computed on a 20 m diameter semi-sphere surrounding the propeller. This blade was characterized by modifications of twist, chord and sweep angle (see Fig. (11(b))) mainly in its outboard part (Fig. (11(a))). In the same paper, the authors argued that the optimization process would have been further enhanced by including, among the design variables, the chord and the twist of the blade sections interacting with the exhaust jet. In addition, it was envisioned that the shape and the position of the exhaust could have a role in further reducing the acoustic impact of the propeller.

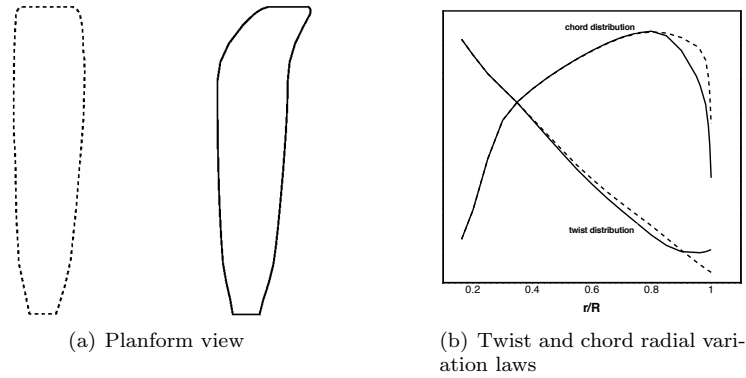


Figure 11. Comparison between reference (dashed line) and *optim-1* (solid line) blades.

The hypothesis according to which the exhausts have a limited impact on the outer part of the blade suggests to decouple the optimization of the inner part of the blade from the outer part. Since the parameterization module allows the user to choose the part of the blade to be parameterized, that part is made coincident with the blade region under the exhaust influence. A DOE based on 100 elements has been scheduled with the "latin-hypercube" method requiring the involvement of the full MDA process. The design variables are the twist and chord at the middle section of the considered region, throughout denoted as T2 and C2, respectively. The parameters T2 and C2 are varied in the ranges $[-40\% : 40\%]$ and $[-25\% : 25\%]$ of their nominal values, respectively.

Fig. (12(a)) shows the combination of T2 and C2 for which the computations are performed, whereas Fig. (12(b)) shows the corresponding results in terms of acoustic energy at the take-off and cruise efficiency. Such a quite computational expensive DOE is exploited in order to generate the surrogate models (RSM)

shown in Fig. (13) to be subsequently used for the optimization.

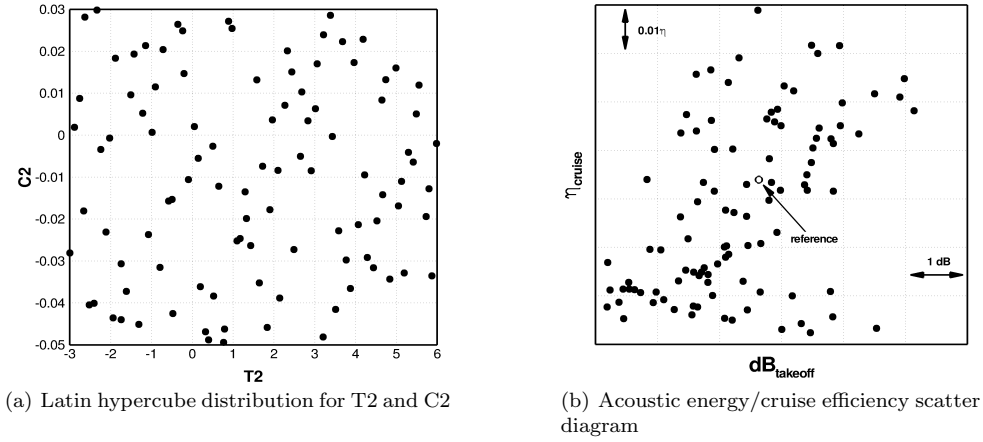


Figure 12. Collection of a DOE results for the inner part of the blade.

By looking at the response surfaces of Fig. (13(a)), it can be observed that a reduction of the acoustic energy is achieved in the region where T2 increases and C2 decreases. On the contrary, as shown by Fig. (13(b)), higher values of T2 tend to downgrade the cruise efficiency and less clear indications can be drawn for the chord influence. Once again, there exist conflicting choices and the multi-objective optimization can play a crucial role in the trade-off analysis.

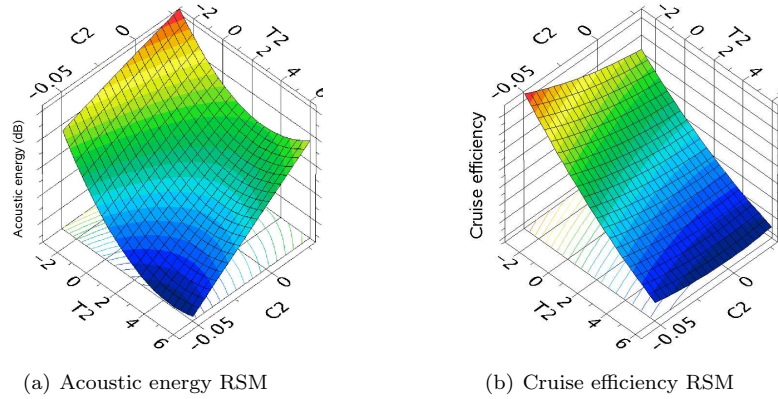


Figure 13. Response surfaces as a function of the design variables T2 and C2.

A multi-objective optimization problem has been set up by requiring the minimization of the acoustic energy and the maximization of the cruise efficiency. The non-dominated sorting evolutionary algorithm (NSEA+) has been used and the objectives were estimated using the RSM surrogate models. The problem has been addressed through the evaluation of 80 designs. The results are shown in Fig. (14) where the designs are collected into a scatter diagram with the objectives on the axes. In this figure the designs falling on the Pareto front are emphasized with black bullets. Among these designs, the design denoted as "*optim-2*" has been selected since it guarantees a reduction of about 1 dB with a small increase in the cruise efficiency.

The *optim-2* blade planform and characteristics are depicted in Fig. (15). As reasonably expected, the optimization process has led to a twist increase and a chord reduction. As a matter of fact, the twist increase tends to counteract the sudden negative variation of the effective angle of attack, whereas the chord reduction tends to diminish the blade-exhaust interaction area.

As far as the exhaust shape and location are concerned, only the variation of the azimuthal relative position has been investigated, since the nozzle shape has an impact on the jet flow properties, while the

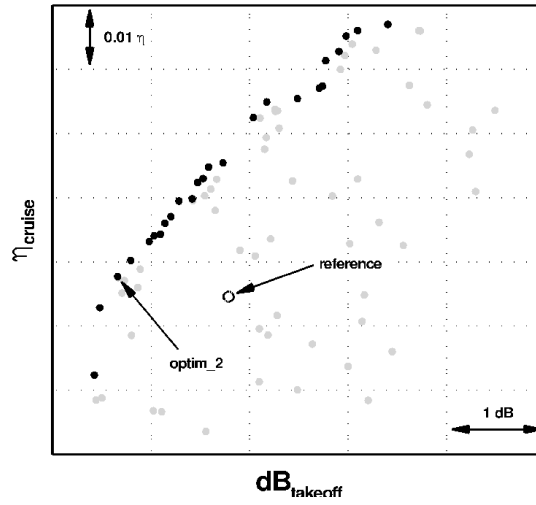


Figure 14. Multi-objective propeller blade optimization results. Overall acoustic energy on the x -axis, aerodynamic cruise efficiency on the y -axis.

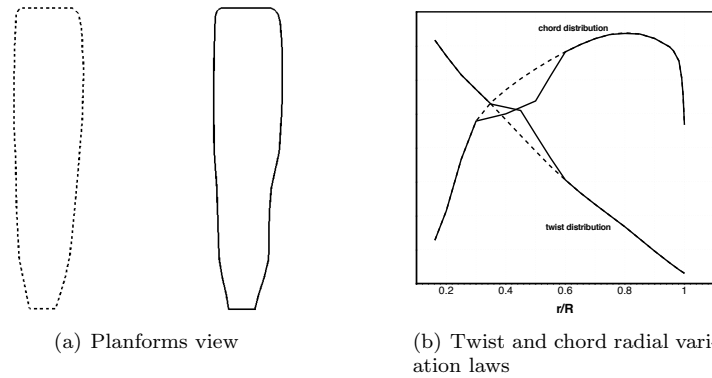


Figure 15. Comparison between reference (dashed line) and *optim-2*(solid line) blades.

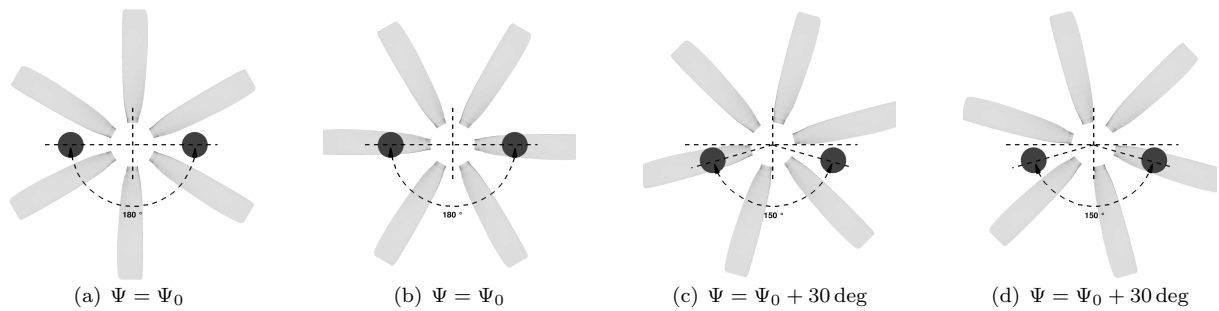


Figure 16. Geometrical considerations about blade-exhaust interaction effects.

radial position results from design considerations related to the blade erosion and de-icing effects due to the jet impingement. Figs. (16(a)) and (16(b)) shows that, for a 6-blade propeller, the baseline configuration characterized by two diametrically opposite exhausts, results in simultaneous passage of two blades through the exhausts. On the contrary, the modified configuration obtained by skewing the azimuthal location of the exhausts, even though it allows to not incur in the above problem, leads to a new distribution of the noise sources, since it may happen that there is always at least a blade under the exhaust influence. For example, Figs. (16(c)) and (16(d)) depict the situation when the minimum angle between the two exhausts is 150 deg. The numerical analysis of this exhaust configuration, which was chosen on the basis of a visual inspection, allows to have a further reduction on the radiated noise at the takeoff (-0.62 dB).

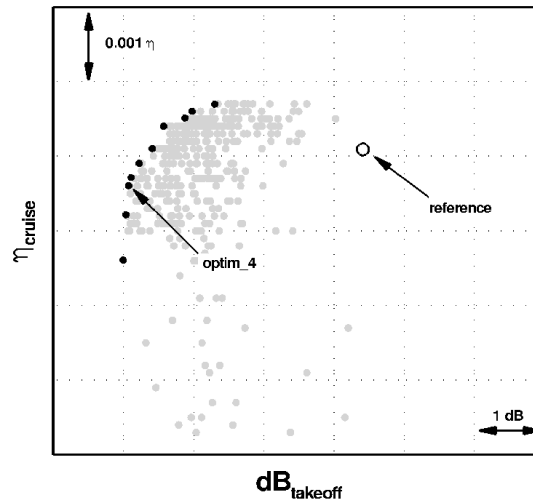


Figure 17. Multi-objective propeller blade optimization results. Overall acoustic energy on the x -axis, aerodynamic cruise efficiency on the y -axis.

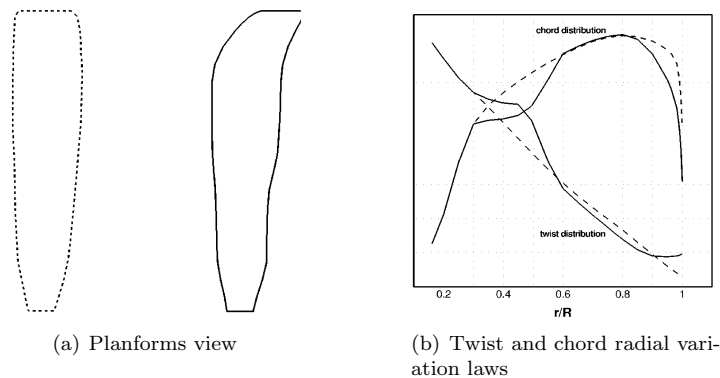


Figure 18. Comparison between reference (dashed line) and *optim-4* blades (solid line).

The optimization of the inboard part of the blade has been obtained under the hypothesis that the inner flow is weakly coupled with the outer one. Hence, by taking advantage from the fact that the *optim-1* blade configuration shares with the reference blade the inboard part, a hybrid design, referred to as "*optim-3*", has been generated replacing in the *optim-1* blade the new designed inboard part of the *optim-2* blade. The analysis of the *optim-3* blade confirms that it can be obtained a reduction of 2.5 dB with respect to the reference blade. However, the blade region under the exhaust influence and the azimuthal position of the exhausts in the propeller disk mutually affect each other. For this reason, by starting from the *optim-3* blade, a new multi-objective problem has been set up for the same objectives; the full MDA process was used with the involvement of three design variables: T2, C2 and the exhaust azimuthal distance $\Delta\Psi$.

It has been necessary to evaluate about 600 designs. These are compared in Fig. (17) in terms of acoustic energy and cruise efficiency and those designs falling on the Pareto front are, as before, emphasized with thicker bullets. From the optima designs on the Pareto front, the "optim-4" blade has been extracted. The geometrical characteristics are illustrated in Fig. (18), whereas the corresponding value of the exhaust azimuthal distance is 162.63 deg.

Table (1) has been filled in with homogeneous results. All of the numerical predictions come from the application of the full MDA process, that is, the design *optim-2* obtained from the RSM evaluations and the *optim-3* hybrid design have been separately re-calculated by using the full MDA process.

Blade	Δ acoustic energy (dB)	Δ cruise efficiency	$\Delta\Psi$ (deg)
Reference	—	—	—
Reference	−0.62	−0.009	30
<i>optim-1</i>	−1.50	+0.006	0
<i>optim-2</i>	−1.10	+0.012	0
<i>optim-3</i>	−2.50	−0.005	0
<i>optim-4</i>	−3.50	−0.0005	17.3

Table 1. Comparison between different blade designs.

VIII. Concluding remarks

The present work was focussed on the aeroacoustic shape optimization of a propeller blade in pusher configuration. An existing methodology was enriched with new modules providing the propeller broadband noise levels. The whole multi-disciplinary computational chain comply with the affordability required by an automatic optimization process. Although broadband noise contributions for rotors and propellers are generally non negligible, in the present study the tonal noise contribution due to the high-speed flow in the tip region and the blade-exhaust interaction in the inner part of the blade, plays a dominant role. The shape optimization revealed that the overall acoustic energy of the pusher propeller can be reduced up to a value of 3.5 dB. This reduction is nearly equally due to an optimal design of the blade planform in the tip and inner regions. Compared to the 5-blade production propeller, the new optimized 6-blade propeller results in a 5.5 dB overall noise reduction. Finally, it is worthwhile to mention that the present analysis did not account for the noise due to the interaction between the propeller blades and the wing wake. This will be the objective of future optimization studies in which use of Navier-Stokes CFD models will be made.

Acknowledgements

This optimization activity has been carried out within the ACADEMIA project (Advanced Computational Aerodynamic Environment for Multi-disciplinary Integrated Analysis) partially funded by the Italian Ministry for Education, University and Scientific Research. The P180 configuration has been provided by Piaggio Aero in the framework of the CESAR project funded by the European Commission.

References

- ¹Pagano, A., Federico, L., Barbarino, M., Guida, F., and Aversano, M., "Multi-objective Aeroacoustic Optimization of an Aircraft Propeller," *AIAA Paper 2008-6059*, September 2008.
- ²Ianniello, S., Mascio, A. D., Salvatore, F., Sollo, A., Aversano, M., and Gennaretti, M., "Evaluation of Noise Excess for Pushing Propeller Aircraft by CFD Aeroacoustic Calculation," *AIAA Paper 2004-3006*, May 2004.
- ³Marulo, F., Sollo, A., Aversano, M., Polimero, U., and Perna, F., "Measurement and Prediction of Community Noise of a Pusher-Propeller General Aviation Aircraft," *AIAA Paper 2005-2984*, May 2005.
- ⁴Pagano, A., Leoncini, P., and Pisoni, A., "System and Software Methodologies Applied to a Rotorcraft Simulation System," *American Helicopter Society Specialists' Meeting, Atlanta, GA (USA)*, November 2000.
- ⁵Le Balleur, J. C., "Viscous-Inviscid Flow Matching: Numerical Method and Applications to Two-Dimensional Transonic and Supersonic Flows," *La Recherche Aéronautique*, Vol. 1978, No. 2, 1978, pp. 67–76.
- ⁶Le Balleur, J. C., "Strong Matching Method for Computing Transonic Viscous Flows Including Wakes and Separations. Lifting Airfoils," *La Recherche Aéronautique*, Vol. 1981, No. 3, May 1981, pp. 21–45.

- ⁷Ffowcs Williams, J. E. and Hawkins, D. L., "Sound Generated by Turbulence and Surfaces in Arbitrary Motion," *Philosophical Transactions of the Royal Society of London, Series A*, Vol. A264, No. 1151, 1969, pp. 321–342.
- ⁸Farassat, F. and Succi, G. P., "The Prediction of Helicopter Discrete Frequency Noise," *Vertica*, Vol. 7, No. 4, 1983, pp. 309–320.
- ⁹Amiet, R. K., "Noise Due to Turbulent Flow Past a Trailing Edge," *Journal of Sound and Vibration*, Vol. 47, No. 3, 1976, pp. 387–393.
- ¹⁰Paterson, R. W. and Amiet, R. K., "Acoustic Radiation and Surface Pressure Characteristics of an Airfoil Due to Incident Turbulence," *NASA CR-2733*, September 1976.
- ¹¹Paterson, R. W. and Amiet, R. K., "Noise of a Model Helicopter Rotor Due to Ingestion of Turbulence," *NASA CR-3213*, 1979.
- ¹²Schlinker, R. H. and Amiet, R. K., "Helicopter Trailing Edge Noise," *NASA CR-3470*, 1981.
- ¹³Roger, M. and Moreau, S., "Broadband Self-Noise from Loaded Fan Blades," *AIAA Journal*, Vol. 42, No. 3, 2004, pp. 536–544.
- ¹⁴Roger, M. and Moreau, S., "Bach-Scattering Correction and Further Extensions of Amiet's Trailing Edge Noise Model, Part 1: Theory," *Journal of Sound and Vibration*, Vol. 286, No. 3, 2005, pp. 477–506.
- ¹⁵Moreau, S. and Roger, M., "Competing Broadband Noise Mechanisms in Low-Speed Axial Fans," *AIAA Journal*, Vol. 45, No. 1, 2007, pp. 48–57.
- ¹⁶Noesisolutions, Belgium, *OPTIMUS, Optimization environment, Software Package, Ver. 5.2*, 2006.
- ¹⁷Samareh, J. A., "Survey of Shape Parameterization Techniques for High-Fidelity Multidisciplinary Shape Optimization," *AIAA Journal*, Vol. 39, No. 5, May 2001, pp. 887–884.
- ¹⁸Hounjet, M. H. L., Le Balleur, J. C., Blaise, D., Bernardini, G., and Pisoni, A., "Maturation of a Full Potential Based Rotors Flow Field Code," *Proceedings of the 26rd European Rotorcraft Forum, The Hague, The Netherlands*, September 2000.
- ¹⁹Miller, J. V., Pidd, M., Pagano, A., Haverdings, H., Bernardini, G., Francescoantonio, P. D., Pisoni, A., and Gracey, M., "ROSAA: The European Solution to Connect Aeroelasticity, Aerodynamics and Acoustic Codes in a Unique User-Friendly Rotorcraft Simulation System," *Proceedings of the 26rd European Rotorcraft Forum, The Hague, The Netherlands*, September 2000.
- ²⁰Le Balleur, J. C. and Girodroux-Lavigne, P., "A Semi-Implicit and Unsteady Numerical Method of Viscous-Inviscid Interaction for Transonic Separated Flows," *La Recherche Aéronautique*, Vol. 1984, No. 1, January 1984, pp. 15–37.
- ²¹Le Balleur, J. C. and Girodroux-Lavigne, P., "Calculation of Dynamic Stall by Viscous-Inviscid Interaction over Airfoils and Helicopter-Blade Sections," *Proceedings of the American Helicopter Society 51st Annual Forum*, 1995.
- ²²Westland, J. and Hounjet, M. H. L., "Clebsch Variable Model for Unsteady Inviscid Transonic Flow with Strong Shock Waves," *AIAA Paper 1993-3025*, 1993.
- ²³Visbal, M. R. and Gaitonde, D. V., "On the Use of High-Order Finite-Difference Schemes on Curvilinear and Deforming Meshes," *Journal of Computational Physics*, Vol. 181, 2002, pp. 155–185.
- ²⁴Daude, F., Lafon, P., Crouzet, F., and Bailly, C., "On Overset Grid Strategy for Aeroacoustics and Aeroelasticity of Moving Bodies," *International Workshop on Fluid-Structure Interaction: Theory, Numerics and Applications Herrsching*, September 2008.
- ²⁵Schulten, J. B. H. M., "Comparison of Measured and Predicted Noise of the Brite-EuRam SNAAP Advanced Propellers," *AIAA Paper 97-1709*, May 1997.
- ²⁶Schultz, K. J., Spletstoesser, W., Junker, B., Wagner, W., Schoell, E., Arnaud, G., Mercker, E., Pengel, K., and Fertis, D., "Parametric Wind Tunnel Test on Rotorcraft Aerodynamics and Aeroacoustics - Test Documentation and Representative Results, HELISHAPE Deliverable HELI/R/5/DLR/06," June 1996.
- ²⁷Leishman, J. G. and Nguyen, K. Q., "State Space Representation of Unsteady Airfoil Behaviour," *AIAA Journal*, Vol. 28, No. 5, September 1990, pp. 836–844.
- ²⁸Leishman, J. G., *Principles of Helicopter Aerodynamics*, Cambridge University Press, 2006.
- ²⁹Schultz, K. J., Spletstoesser, W., Junker, B., Wagner, W., Schoell, E., Arnaud, G., Mercker, E., Pengel, K., and Fertis, D., "Wind Tunnel Model Database, HeliNOVI Report D2.1-1," 2002.
- ³⁰Fitzpatrick, J. A., "Aeroacoustics Research in Europe: The CEAS-ASC Report on 2004 Highlights," *Journal of Sound and Vibration*, Vol. 288, No. 1-2, 2005, pp. 1–32.
- ³¹Ianniello, S., "An Algorithm to Integrate the FW-H Equation on a Supersonic Rotating Domain," *AIAA Journal*, Vol. 37, No. 9, September 1999, pp. 1040–1047.
- ³²Ianniello, S., "Quadrupole Noise Predictions Through the Ffowcs WilliamsHawkings Equation," *AIAA Journal*, Vol. 37, No. 9, September 1999, pp. 1048–1054.
- ³³Di Francescantonio, P., "A New Boundary Integral Formulation for the Prediction of Sound Radiation," *Journal of Sound and Vibration*, Vol. 202, No. 4, 1997, pp. 491–509.
- ³⁴Brentner, K. S. and Farassat, F., "Analytical Comparison of the Acoustic Analogy and Kirchhoff Formulation for Moving Surfaces," *AIAA Journal*, Vol. 36, No. 8, 1998, pp. 1379–1386.
- ³⁵Brentner, K. S., "Numerical Algorithms for Acoustic Integrals with Examples for Rotor Noise Prediction," *AIAA Journal*, Vol. 35, No. 4, 1997, pp. 625–630.
- ³⁶Casalino, D., "An Advanced Time Approach for Acoustic Analogy Predictions," *Journal of Sound and Vibration*, Vol. 261, No. 4, 2003, pp. 583–612.
- ³⁷Rozenberg, Y., *Modélisation Analytique du Bruit Aérodynamique à Large Bande des Machines Tournantes: Utilisation de Calculs Moyennés de Mécanique des Fluides*, Ph.D. thesis, Ecole Centrale de Lyon, December 2007.
- ³⁸Brooks, T. F. and Hodgson, T. H., "Trailing Edge Noise Prediction from Measured Surface Pressures," *Journal of Sound and Vibration*, Vol. 78, No. 1, 1981, pp. 69–117.